

# Ultrabroadband Resonant Frequency Doubling on a Chip

Marco Clementi,<sup>1,\*</sup> Luca Zatti,<sup>2</sup> Ji Zhou,<sup>1</sup> Marco Liscidini,<sup>2</sup> and Camille-Sophie Brès<sup>1</sup>

<sup>1</sup>*Photonic Systems Laboratory, École Polytechnique Fédérale de Lausanne, 1015 Lausanne, Switzerland*

<sup>2</sup>*Dipartimento di Fisica, Università di Pavia, Via A. Bassi 6, 27100 Pavia, Italy*

(Dated: December 5, 2024)

Microresonators are powerful tools to enhance the efficiency of second-order nonlinear optical processes, such as second-harmonic generation, which can coherently bridge octave-spaced spectral bands. However, dispersion constraints such as phase-matching and doubly resonant conditions have so far limited demonstrations to narrowband operation. In this work, we overcome these limitations showing ultrabroadband resonant frequency doubling in a novel integrated device, wherein the resonant enhancement of pump and second harmonic are individually addressed in two distinct and linearly uncoupled microring resonators, each adjusted to target the respective spectral band. The two microresonators are designed and tuned independently, yet share a common interaction region that grants nonlinear coupling over a quasi-phase-matching bandwidth exceeding 200 nm, enabled by the inscription of a photoinduced  $\chi^{(2)}$  grating. The system allows to not only conveniently disentangle the design parameters of the two microresonators but also to reconfigure the doubly resonant condition electrically, and the phase-matching condition optically. We demonstrate milliwatt-level addressable second-harmonic generation over the entire telecom band and then configure the device to generate and upconvert a Kerr frequency comb with bandwidth exceeding 100 nm and upconverted power up to 10 mW.

Second-order nonlinear optical processes, such as second-harmonic generation (SHG), are fundamental tools in photonics technology, as they enable converting light across widely separated regions of the optical spectrum while preserving its coherence [1]. They find widespread application in the engineering of light sources [2], imaging [3], ultrafast physics [4], material science [5], and quantum technology [6], to name a few. Leveraging the nonlinear dielectric response of a medium typically requires high field intensities, which nowadays can be effectively achieved through high peak power pulsed sources in bulk systems — or by exploiting spatial and temporal light confinement in integrated structures.

Microring resonators stand, among various microcavity geometries proposed [7, 8], as a prime choice for efficient on-chip frequency doubling, thanks to the possibility to design devices with high Q resonances at both fundamental- (FH) and second-harmonic (SH). Highly efficient frequency doubling has notably been achieved in  $\chi^{(2)}$  material platforms such as thin-film lithium niobate (TFLN), with conversion efficiency ( $CE = P_{SH}/P_{FH}^2$ ,  $P_{FH}$  and  $P_{SH}$  being respectively the pump and SH power) as high as 5,000,000%/W [9], III-V materials (e.g. AlN [10], GaN [8], GaAs [11], GaP [12]), and silicon carbide (SiC) [13]. Despite remarkable advances, these materials generally still suffer from limited power handling capability, a non-standardized fabrication process, and material-specific limitations.

An alternative approach is represented by silicon nitride ( $\text{Si}_3\text{N}_4$ ) integrated photonics [14], which combines low loss, a well-established and CMOS-compatible fabrication, and excellent power handling capabilities. Although lacking intrinsic  $\chi^{(2)}$  due to its amorphous nature,  $\text{Si}_3\text{N}_4$  can be endowed with a photoinduced second-order nonlinearity through the coherent photogalvanic effect [15–18]. In resonant structures, this can yield high CE

(up to 2,500%/W) [19] and record-high generated power (>10 mW) [20]. These advances have made it possible to realize complex chip-scale functionalities such as frequency comb self-referencing [17, 21] and self-injection-locked SHG [22, 23].

While microring resonators are capable of highly efficient frequency doubling, their practical usage is hindered by limitations in bandwidth and poor wavelength tunability. Indeed, broadband SHG in a ring resonator must satisfy three requirements simultaneously: (i) phase-matching, (ii) doubly resonant condition for pump and SH, and (iii) free spectral range (FSR) matching. Perfect phase-matching is usually prevented by material and modal dispersion, but it can be obtained through intermodal phase-matching [19] or through quasi-phase-matching (QPM) — the latter either exploiting the natural birefringence of the medium (4-QPM) [11] or the electric-field poling of a ferroelectric waveguide [9]. Doubly resonant high-Q microrings are also typically unachievable deterministically, even by tailored designs, due to fabrication tolerances, for the resonance position must be controlled with a precision comparable with the linewidth. A common workaround is thermal tuning [24], where the slightly different thermo-optic effect on pump and SH resonances can compensate for small deviations from a nearly doubly resonant condition statistically obtained among many fabricated samples. However, this method is not scalable, does not allow for the precise control of the operation wavelength, and becomes unpractical in systems with large free spectral range (FSR). If a doubly resonant condition is difficult to achieve at a given pump wavelength, broadband SHG involving multiple resonances is even more challenging. Indeed, the FSRs at pump and SH frequencies are in general different: therefore, high-Q resonators only enable doubly resonant SHG over a small number of resonances at the

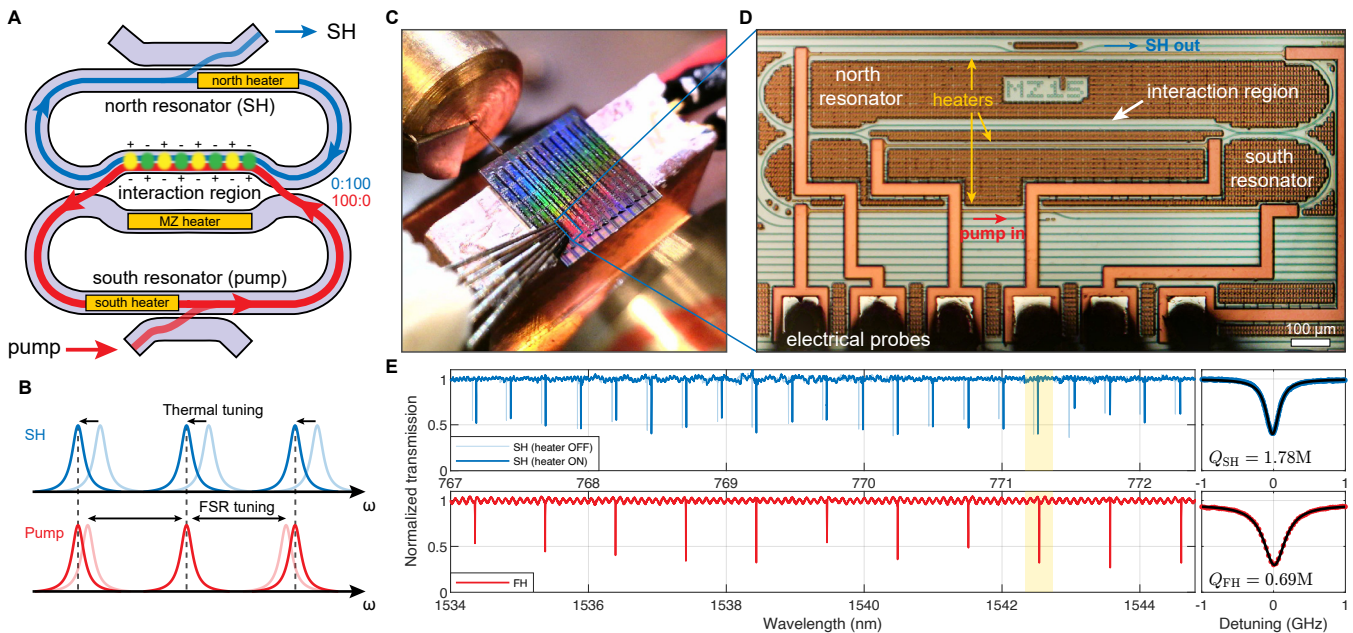


FIG. 1. **Reconfigurable frequency doubling device.** **a.** Conceptual schematic of the device. The pump and SH circulate respectively in the south and north loops, sharing a fraction of the optical path where nonlinear interactions (AOP and SHG) occur. **b.** Resonances distribution for the north (*top*) and south (*bottom*) resonators, respectively at the pump and SH frequencies. The absolute resonance frequencies in the north (south) ring can be tuned by acting on the north (south) heater. The resonators' FSR can be individually tuned by tailoring the respective loop length. **c.** Micrographs of the fabricated chip and **d.** a single device. **e.** Low power transmission spectra for the  $TE_{00}$  mode in the SH (*top*) and pump (*bottom*) bands. The detail shows a typical pair of resonances involved in the SHG process and associated Lorentz fit.

time, restricting applications such as frequency comb up-conversion to a limited number of spectral lines [25, 26] and, more generally, setting a trade-off between bandwidth and CE [27–29]. In principle, this can be mitigated by adjusting the waveguide cross-section to match the group velocity [21], but at the cost of dispersion engineering, which is already required for controlling the comb properties or generating soliton states.

In this work, we address all of these issues, inherent to the single-ring approach, by demonstrating a device where the pump and SH fields are associated with two separate resonators that yet share a common path where nonlinear processes can occur. This change of paradigm allows one to adjust the optical properties of the system in different spectral regions independently and achieve efficient nonlinear interaction without dispersion engineering [30–35]. First, a photoinduced nonlinearity is realized in the  $Si_3N_4$  coupling region where pump and SH coexist, whose periodicity automatically satisfies the QPM condition over a broad bandwidth (all-optical poling process, AOP [20]). Second, the families of azimuthal modes of the two resonators can be independently tuned through electric actuators to make sure that a doubly resonant condition is always satisfied. Third, the microresonator lengths are tailored to grant FSR matching at the design level. Finally, efficient in-coupling and extraction of light at the pump and SH wavelength are obtained by optimizing the couplers to the two resonators inde-

pendently. We investigate the device operating principle by two-photon microscopy, showing that the AOP process occurs in the region where the circulating pump and SH field interact, proving the linearly uncoupled nature of the two resonators. We then showcase the potential of this approach by reconfiguring the device to achieve SHG with milliwatt-level generated power over the C and L telecom bands, limited only by the bandwidth of our amplifiers. Finally, we demonstrate the broadband operation of the device by using it to generate a modulation instability comb that we frequency-double within a pump bandwidth of nearly 100 nm (12.5 THz).

## RESULTS

### Device description and operating principle

A conceptual schematic of the reconfigurable SHG source is shown in Fig. 1a. The device is composed of two “race-track” resonators designed to operate respectively in the pump (“south”) and SH (“north”) spectral bands. Both resonators are critically coupled to their bus waveguide for the fundamental transverse-electric mode ( $TE_{00}$ ). A Mach-Zehnder interferometer (MZI) structure is used to introduce an interaction region between the two resonators by using two directional couplers designed to operate near 100:0 splitting ratio in the pump band and

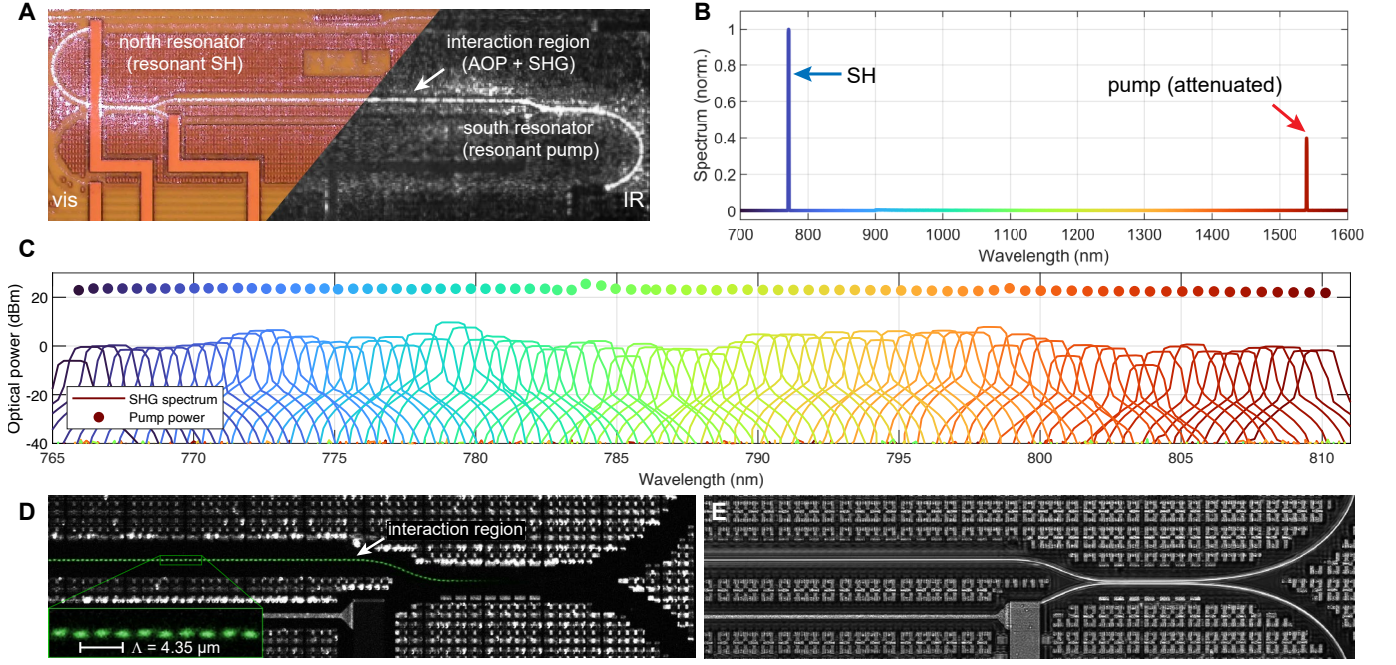


FIG. 2. **All-optical poling and second-harmonic generation.** **a.** Micrograph of a typical device in frequency doubling operation. The visible camera (*left*) emphasizes the resonant field enhancement of the generated SH in the north loop, while the infrared (IR) camera (*right*) shows the field enhancement in the south loop. Note that the two fields overlap in the shared path, where AOP and simultaneous SHG occur. **b.** Typical SHG spectrum. **c.** Collection of SHG spectra associated with pumping in the C and L bands (resolution: 1 nm). Each trace is a detail of a spectrum as shown in panel b. The heater currents are slightly adjusted for each data point to optimize the generated power. **d.** Two-photon and **e.** one-photon micrograph of one of the devices after inscription of the nonlinear QPM grating through AOP. TPM imaging reveals a periodic  $|\chi^{(2)}|^2$  distribution that only exists in the interaction region, confirming the linearly uncoupled nature of the process.

near 0:100 in the SH band [35]. Finally, a thermo-optic phase shifter (“heater”) is placed on each resonator and on the lower arm of the MZI, allowing, respectively, to tune the set of resonant modes at pump/SH and to compensate for any residual linear coupling between the two racetracks.

The resulting resonances distribution is sketched in Fig. 1b: differently from the case of a single resonator, the two sets of modes can be independently shifted to achieve a doubly resonant condition by acting on the north/south heater. Moreover, by engineering the length of the two resonators, one can by-design match the FSRs of the two rings in order to allow simultaneous frequency doubling on multiple resonances, according to the formula:

$$\text{FSR}_{\text{FH}} = \frac{v_g^{\text{FH}}}{L_{\text{FH}}} = \frac{v_g^{\text{SH}}}{L_{\text{SH}}} = \text{FSR}_{\text{SH}} \quad (1)$$

where  $v_g^{\text{FH(SH)}}$  is the group velocity of the pump (SH) mode and  $L_{\text{FH(SH)}}$  is the optical path length of the south (north) resonator. Note that in the case of a single resonator (where  $L_{\text{FH}} = L_{\text{SH}}$ ), FSR matching can only be achieved through group velocity matching, posing a significant constraint on dispersion engineering.

A typical fabricated device is shown in Figs. 1c-d. We use a lensed fiber to couple light to the chip and electrical probes to actuate the heaters (see Methods). Typi-

cal transmission spectra in the pump and SH bands are shown in Fig. 1e. By acting on the south and north resonator heaters we are able to observe a rigid and independent shift of the respective resonance spectra (the north heater case is shown in Fig. 1e). Similarly, acting on the MZI heater enables us to dynamically vary the pump resonances visibility and linewidth, as a result of power leakage to the north resonator, strongly over-coupled at the FH (see Supplementary Note 1). Once these values are optimized, from best fit of the Lorentzian lines recorded we estimate a loaded Q factor of around  $0.69 \times 10^6$  at the pump and  $1.78 \times 10^6$  at the SH.

### Addressable doubly resonant SHG

To investigate SHG, we pump the south resonator with an amplified tunable laser and configure the device with the procedure described in the Methods. The occurrence of the AOP process is marked by a sudden increase of the SHG power from the north resonator. Visible and infrared imaging of the device in operation (Fig. 2a) provides straightforward evidence of the linearly uncoupled nature of the process. Light scattering from the north and south resonators during the SHG process, when acquired with either a visible or an infrared camera, sug-



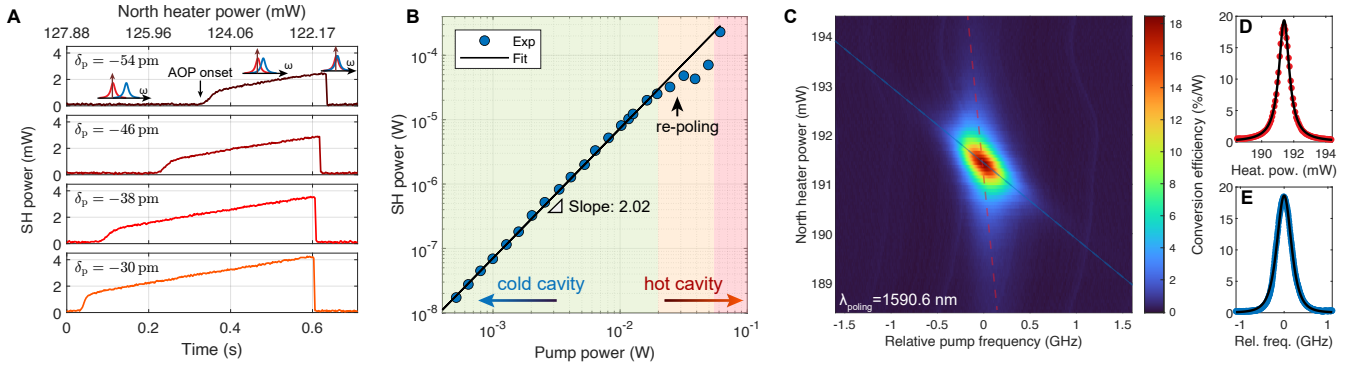


FIG. 3. **Reconfiguration of the nonlinear interaction.** **a.** SHG traces obtained by ramping down the north heater power (i.e. slowly blue-shifting the north ring SH resonance). Each trace corresponds to a different detuning  $\delta_p = \lambda_{\text{res}} - \lambda_{\text{pump}}$  of the pump laser from the hot cavity resonance at its maximal shift. The asymmetric lineshape is attributed to the presence of thermal shift in the north resonator. **b.** SHG power scaling measurement and quadratic fit. **c.** High resolution SHG map at in the cold cavity regime after inscription of the nonlinear grating. Here the pump power is kept low (0.2 mW) to prevent thermal shifts as well as the triggering the AOP process. The red and blue dashed lines highlight respectively the pump and SH resonance peaks, which red-shift for increasing north heater power. The peak values are plotted in panels **d** and **e** and fitted with a Lorentzian and squared Lorentzian function respectively (black solid line).

gests that the SH and pump fields are circulating only in their respective resonators. A typical spectrum of the output light is also shown in Fig. 2b, confirming the SHG process and the absence of spurious spectral components. By repeating this procedure, we reproduce a similar result among several devices with different FSR and coupling conditions, systematically recording a generated SH power of up to 10 mW.

We then focus our attention on a single device, characterized by a nominal FSR of about 130 GHz, and investigate its suitability for efficient SHG across multiple resonances. To this end, we tune the pump wavelength to each of the resonances within the C and L telecom bands (1530-1620 nm) and repeat the optimization procedure, each time reconfiguring the QPM grating by AOP. Fig. 2c shows the recorded SHG spectra, all corresponding to an output power in the milliwatt level (average: 1.4 mW), proving the capability of the integrated nonlinear device to operate across a wideband range when electrically reconfigured. Note that this demonstration is limited by the availability of amplifiers, while the nonlinear device is expected to be capable of covering an even broader spectrum, limited only by the bandwidth of the resonators' point couplers and of the MZI, estimated at about 150 nm (19 THz).

Further insight on the AOP process can be gathered by two-photon microscope (TPM) imaging of the inscribed  $\chi^{(2)}$  grating (Fig. 2d) [17, 36]. Compared with regular (one-photon) micrographs (Fig. 2e), TPM images clearly show that the nonlinear grating inscription occurs only in the upper arm of the interferometer, corroborating the hypothesis of linear uncoupling. The poling period is measured to be around  $4.35 \mu\text{m}$ , in perfect agreement with the simulated values of effective indices for the  $\text{TE}_{00}/\text{TE}_{00}$  mode pair at pump/SH.

## Nonlinear properties

To gather insight on the nonlinear properties of the developed device, we first perform a broadband mapping of the AOP process [22, 24], as detailed in Supplementary Note 2. We then focus our attention on a single resonance (around 1590 nm) and investigate the AOP dynamics at different values of pump detuning (Fig. 3a). We first set the pump wavelength close to resonance, and then slowly ramp down the north heater power, inducing a blue-shift of the SH resonance. Consequently, the SH field enhancement is progressively increased until a sudden spike in the SH power is observed, marking the AOP onset, where the conditions for poling of the north resonator are met [20]. When further decreasing the north heater power, the generated SH increases owing to the increased field enhancement, until a sudden drop is observed. We attribute this to the specific dynamics of the AOP process in resonant structures [37]. We repeat the measurement while further tuning the pump close to resonance, observing an earlier occurrence of the AOP onset, an overall increase of the peak generated SH, and a systematic drop occurring at nearly the same SH detuning conditions.

The experiments described so far entail circulating pump and SH intensities sufficiently high to trigger the AOP process. However, it is known that the  $\chi^{(2)}$  grating, once inscribed, can subsist for very long time, exceeding several months at room temperature [36]. We therefore investigate the nonlinear response of the system in a regime of low pump power, insufficient to trigger the erasure or reconfiguration of the grating, after previous poling a selected resonance. To establish the limits of such “cold cavity” regime, we perform a scaling analysis of the generated SH power as a function of the pump power in the bus waveguide, as shown in Fig. 3b. For each value of the pump power, the wavelength is slowly



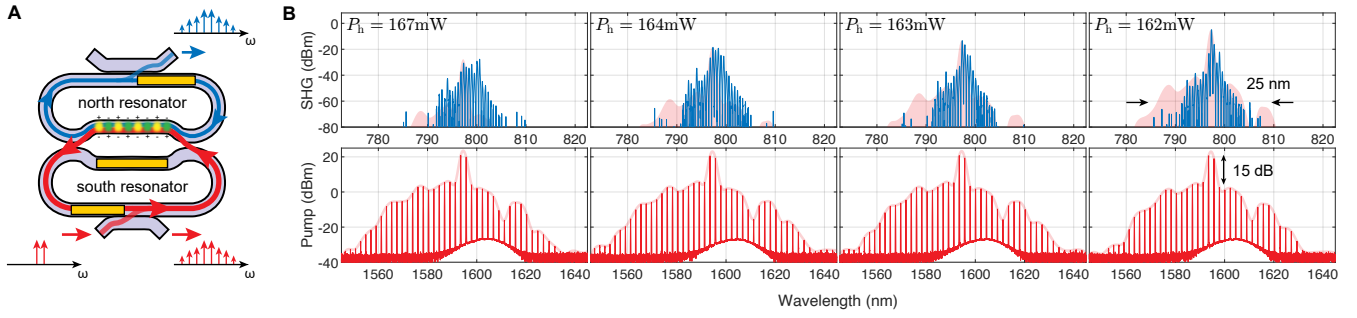


FIG. 4. **Stimulated FWM comb upconversion.** **a.** Schematic of the stimulated FWM comb generation. The south loop is fed with a bichromatic pump created by mixing and amplifying two tunable sources spaced at a multiple of the FSR. The resonantly enhanced  $\chi^{(3)}$  interaction in the south resonator produces an incoherent comb through cascaded FWM. The comb is then frequency doubled in the interaction region, where it participates to AOP and related SHG and SFG, and finally output from the north resonator coupler. **b.** Generated comb (spacing: 2 FSR) for varying resonance detuning configurations. When red-detuning the north ring resonances from the optimal condition, the entire SHG comb power is gradually decreased. The shaded area in the top graphs represent the squared FH comb envelope (shaded trace in the bottom graphs) rescaled to the maximum of the generated SH, for comparison.

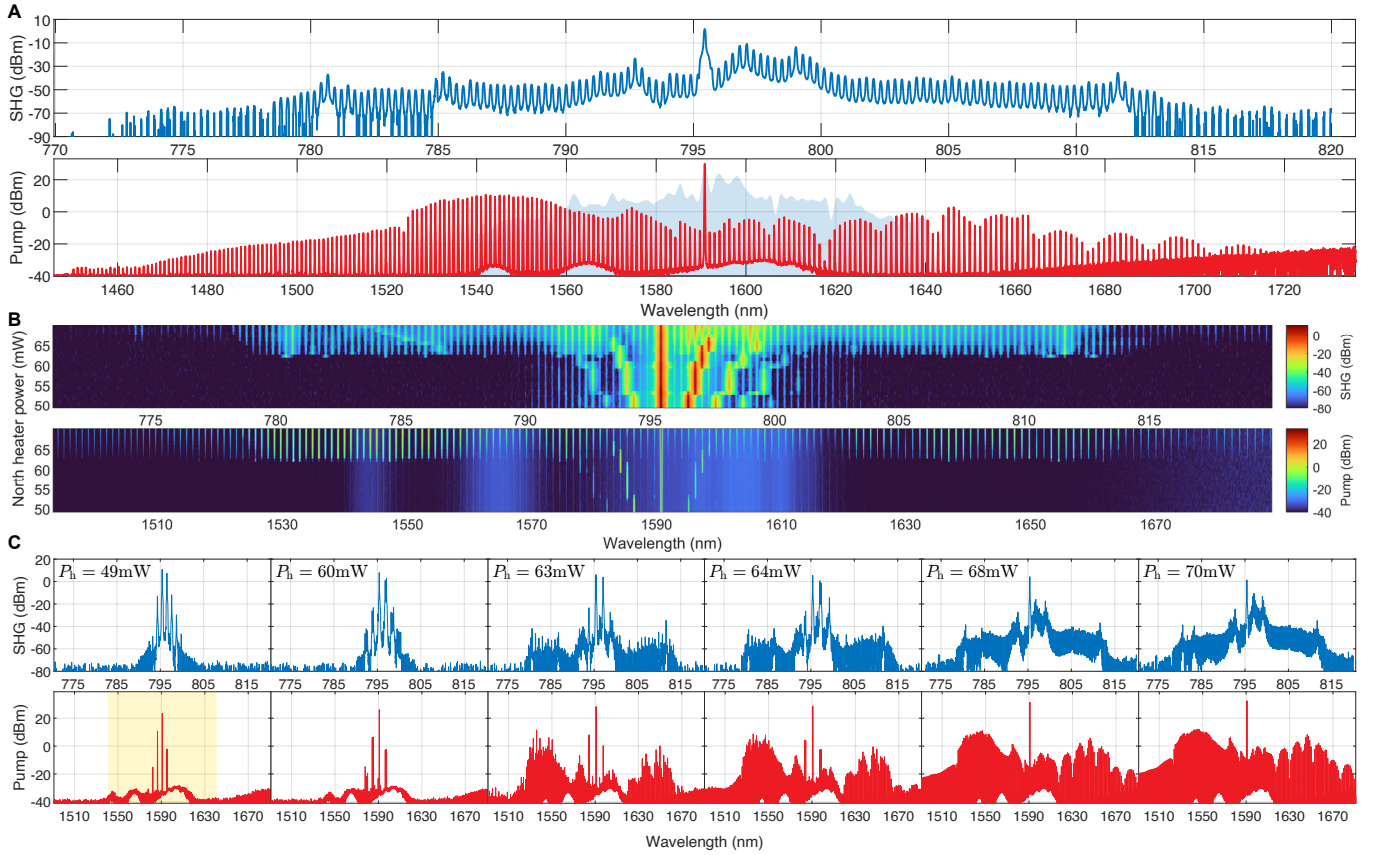


FIG. 5. **Modulation instability comb generation and upconversion.** **a.** Generated MI comb (*bottom*) and its upconverted spectrum (*top*), with a pump power of 1.6 W. The shaded yellow area corresponds to the upconverted spectrum extent. **b.** Accumulated optical spectra of FH (*bottom*) and SH (*top*) for varying north heater power. A crossover from Turing patterns to the broadband MI comb can be observed in combination with a decrease of the overall generated power. **c.** Selected spectra from panel **b**.

scanned through the resonance from the blue to the red side, and the peak SHG power is recorded. The resulting trend shows a quadratic increase of the generated SH for

pump powers below approximately 20 mW. When the pump power is further increased, a deviation from such trend is recorded: we attribute this to the reconfiguration

of the  $\chi^{(2)}$  grating. When further increasing the pump power, the generated SH restores the quadratic trend, reentering the combined AOP/SHG process (“hot cavity” regime). The cold- and hot-cavity regimes are therefore desirable for efficient SHG, while the intermediate regime of reconfiguration should be avoided.

With these results in hand, we investigate the SHG process in the cold cavity regime, for which we map the CE as a function of the pump wavelength and north heater power after poling (Fig. 3c). To minimize the impact of thermal bistability on the measurement, here we keep the pump power as low as 0.2 mW. The result displays two main branches: the first (red dashed line), nearly vertical, represents the pump resonance, which doesn’t undergo a shift when increasing the north heater power (except for a slight thermo-optic crosstalk); the second (blue dashed line), oblique, is associated with the SH resonance, which experiences the most important shift rate. In Figs. 3d-e we show the slices obtained along these trends, which we fit with a Lorentzian and squared-Lorentzian model respectively.

### Frequency comb upconversion

To showcase the potential of our device, we investigate its suitability for upconversion of a frequency comb. We first inject in the south resonator two separate L band CW lasers, amplified and tuned to match an integer multiple of the resonator’s FSR, as sketched in Fig. 4a, and tune the south resonator heater in order to couple efficiently to the respective resonances. Enhanced by the south resonator, the circulating field produces a cascade of stimulated four-wave mixing (FWM) processes, resulting in the formation of an incoherent frequency comb, whose bandwidth is determined by the pump line spacing, detuning, and waveguide dispersion.

The circulating FWM comb can trigger the AOP process. To this end, we slowly decrease the north heater power while monitoring the generated spectrum at both pump and SH with two optical spectrum analyzers (OSA), as shown in Fig. 4b. As soon as the appropriate detuning conditions are met, the north resonator is observed to scatter near-visible light, confirming the onset of the AOP process. The SHG spectrum displays a set of equally spaced comb lines with the same frequency spacing (1/4 wavelength spacing) as the pump, and upconverted power in the milliwatt level per line. We interpret the observed spectrum as the result of a combination of SHG and SFG processes, all phase matched by the same  $\chi^{(2)}$  grating, made possible by the matching of the two resonators’ FSRs, which do not affect the pump spectrum.

The envelope of the frequency doubled comb systematically replicates that of the pump spectrum squared (red shaded area), as expected, with a small deviation that we attribute to the residual FSR mismatch and to the effect of GVD. Note that, in contrast, the QPM band-

width (estimated around 202 nm) does not limit the generation bandwidth, owing to the short length of the grating  $L_{\text{MZI}} \approx 361 \mu\text{m}$  (see Methods, Eq. 2). By varying the comb lines spacing to integer multiples of the FSR, it is also possible to broaden the fundamental comb (Supplementary Note 3), while the frequency doubling bandwidth remains nearly constant.

### Simultaneous comb generation and upconversion

We then investigate the system suitability to simultaneously generate and upconvert a Kerr comb. To this end, we use a single high-power (1.6 W) line around 1591 nm to pump the south resonator and produce a modulation instability (MI) comb (Fig. 5a). To trigger the comb and maximize its extent, we deliberately introduce a weak linear coupling between the north and south resonators (Supplementary Note 4), which produces an anticrossing-type perturbation in the otherwise normal GVD profile [38] and simultaneously broadens the linewidth of higher-frequency resonances, until we establish an optimal span of around 300 nm. By adjusting the north heater power to reach a doubly resonant condition, an upconverted comb spectrum spanning nearly 50 nm is observed in the SH band, corresponding to a 100 nm extent in the pump band. The upconverted comb spectrum replicates the envelope of the pump comb, but compared to the FWM cases, the pump comb shape also depends on the north heater power, as shown in (Figs. 5b-c). We see that a lower heater power (lower SH detuning, while keeping unchanged the excitation conditions) results in the most efficient SHG, with upconverted power exceeding 10 mW per line (Figs. 5c, first panel), but at the same time a generated comb spectrum of only few lines, characteristic of primary combs. When increasing the heater power, hence increasing the SH detuning, we observe a gradual transition towards the full MI comb formation at the pump band and broader upconversion, albeit paired with a decrease in the overall upconverted power. This phenomenological trade-off trend can be attributed to pump depletion, which sets a competition between the  $\chi^{(3)}$  process yielding the comb formation and the AOP/SHG process.

## DISCUSSION

The device developed represents the first demonstration of addressable doubly resonant SHG through external tuning, overcoming several fundamental limitations inherent in the single-resonator approach. Our strategy can be generally set in the context of coupled resonator systems (or “photonic molecules”) which have been recently employed to improve the performance of other nonlinear processes, such as comb generation [42], self-injection locking [43], and quantum light generation [44, 45]. However, our approach differs fundamentally from the above

TABLE I. Comparison of state-of-the-art integrated platforms for SHG at telecommunication wavelength.

Platform	On-chip CE (%/W)	SHG bandwidth (nm)	Max on-chip SH power (mW)	Phase-matching method
TFLN waveguide ( <i>X</i> -cut) [39]	9,500	0.97	16.5	QPM (electric field poling)
TFLN microring ( <i>Z</i> -cut) [40]	250,000	>10	0.1	QPM (electric field poling)
TFLN microring ( <i>Z</i> -cut) [9]	5,000,000	0.005 <sup>a</sup>	0.02	QPM (electric field poling)
TFLN microring ( <i>Z</i> -cut) [28]	n.a.	80 <sup>b</sup>	n.a.	n.a.
AlN microring [41]	2,500	0.42	3.3	Intermodal
AlN microring [10]	17,000	5	11	Intermodal
AlN microring [27]	7	60 <sup>b</sup>	0.61	Intermodal
GaP microdisk [12]	38	1	$4 \times 10^{-5}$	$\bar{4}$ -QPM
GaP microring [29]	n.a.	40 <sup>b</sup>	n.a.	n.a.
SiC microring [13]	360	0.03 <sup>a</sup>	0.001	Intermodal
Si <sub>3</sub> N <sub>4</sub> waveguide [15]	0.05	4.5	0.16	QPM (all-optical poling)
Si <sub>3</sub> N <sub>4</sub> waveguide [21]	0.15	>25	n.a.	QPM (all-optical poling)
Si <sub>3</sub> N <sub>4</sub> waveguide [17]	0.003	>100	0.6 <sup>c</sup>	QPM (all-optical poling)
Si <sub>3</sub> N <sub>4</sub> microring [25]	0.16	10 <sup>b</sup>	1	Intermodal
Si <sub>3</sub> N <sub>4</sub> microring [19]	2,500	0.06 <sup>a,d</sup>	2.2	Intermodal
Si <sub>3</sub> N <sub>4</sub> microring [20]	47.6	0.6 <sup>a,d</sup>	12.5	QPM (all-optical poling)
Si <sub>3</sub> N <sub>4</sub> microring [24]	2	2.3	2	QPM (all-optical poling)
<b>Si<sub>3</sub>N<sub>4</sub> microresonators system (this work)</b>	<b>40</b>	<b>&gt;100<sup>b</sup></b>	<b>&gt;10</b>	<b>QPM (all-optical poling)</b>

The shaded area highlights silicon nitride photonic platforms. The bandwidth is estimated at 10 dB; power and CE are intended at CW regime unless otherwise stated. n.a.: data not available.

<sup>a</sup> Doubly resonant SHG limited to a single resonance pair at pump/SH.

<sup>b</sup> Estimated from the overall extent of the upconverted comb spectrum.

<sup>c</sup> Average value at pulsed regime.

<sup>d</sup> With thermal tuning of the resonance.

due to the deliberate choice of eliminating the linear coupling, with the advantages of (i) strongly suppressing the parasitic loss due to overcoupling of north resonator's modes at the pump (ii) avoiding the formation of supermodes, associated with a lower field enhancement (equivalently, larger mode volume) and (iii) avoiding (or controlling) alterations to the dispersion profile associated with mode anti-crossings.

This strategy, originally introduced in the context of spontaneous parametric sources [30–34] and here combined with AOP, enables electrical control over the doubly resonant condition within a pump bandwidth exceeding 90 nm (11.2 THz), only limited in this demonstration by the range of our amplifiers. The system can systematically generate milliwatt-level powers, with CE as high as 40%/W in CW regime. These values are already useful for several practical applications and can likely be improved through further reduction of the propagation loss and by achieving a better rejection of the residual linear and intermodal coupling at the pump, further mitigating the need for high pump power.

Moreover, our device enables the broadband upconversion of frequency combs through the engineering of a “synthetic” group velocity matching condition (Eq. 1), which we showcase over a pump bandwidth of about 100 nm (12.5 THz) and upconverted power exceeding 10 mW per line, with potential applications to self-referencing of frequency combs. While it is worth noting that few earlier demonstrations using the single resonator approach have already shown comparable upconversion bandwidth [27–29], the generated powers reported so far have always been at least two orders of magnitude lower

than in the present demonstration, and the nature of the modes involved at the SH has not always been clarified.

Table I provides an overview of several integrated platforms at the state of the art, showing the key figures of merit for broadband SHG. While some demonstrations have reported higher values separately, our result effectively represents the best trade-off between CE, bandwidth, and generated power, especially among CMOS-compatible platforms.

While the present demonstration focused on the SHG and SFG processes, the same device can be used to withstand downconversion processes such as difference frequency generation [46] and spontaneous parametric downconversion [47], or embedded in more complex photonic systems such as hybrid self-injection-locked sources [22]. Finally, this approach is universal and could be extended to different material platforms, such as TFLN, in combination with an appropriate strategy to address the QPM condition [9].

In conclusion, we have demonstrated a frequency doubling device capable to arbitrarily address the doubly resonant condition, unlocking the potential for broadband and efficient upconversion. Our approach can be extended to a variety of nonlinear integrated systems and processes, with applications ranging from microcombs to on-chip nonclassical light sources.

## Methods

**Theoretical model.** In order to estimate the generated power, we can derive an equation for the SHG process. Considering the general expression for the second order nonlinear Hamiltonian, as given in [48], the fields of interest are those inside the upper arm of



the Mach-Zehnder interferometer at the fundamental and second-harmonic frequencies and, if we explicit the terms in the equation, following the backward Heisenberg picture [49] and consider the CW regime, we get for the power of the generated second harmonic:

$$P_{\text{SH}} = \frac{\left(\chi_{\text{eff}}^{(2)} P_{\text{FH}}\right)^2 \omega_{\text{SH}} \omega_{\text{FH}} |J(\omega_{\text{SH}}, \omega_{\text{FH}}, \omega_{\text{FH}})|^2}{4\epsilon_0 n_{\text{eff,SH}}^2 n_{\text{eff,FH}}^4 v_{\text{g,SH}} v_{\text{g,FH}}^2 A_{\text{eff}}}, \quad (2)$$

where  $\chi_{\text{eff}}^{(2)}$  is the second order nonlinear susceptibility induced by the AOP,  $P_{\text{FH}}$  is the injected pump power (in the bus waveguide),  $n_{\text{eff}}$  is the effective index and  $v_{\text{g}}$  is the group velocity (at the FH/SH frequency),  $A_{\text{eff}}$  is the nonlinear effective area of the process, and  $J(\omega_{\text{SH}}, \omega_{\text{FH}}, \omega_{\text{FH}})$  is the overlap integral, which takes into account the spatial overlap of the three fields involved in the process, that in our structure interact only inside the upper arm of the MZI of length  $L_{\text{MZI}}$ , and is given by:

$$J(\omega_{\text{SH}}, \omega_{\text{FH}}, \omega_{\text{FH}}) = f_{\text{north}}(\omega_{\text{SH}}) f_{\text{south}}(\omega_{\text{FH}})^2 e^{i \frac{\Delta k L_{\text{MZI}}}{2}} \times \text{sinc}\left(\frac{\Delta k L_{\text{MZI}}}{2}\right) [-\sigma_{\text{SH}} \kappa_{\text{FH}}^2 + i \sigma_{\text{FH}}^2 \kappa_{\text{SH}}] L_{\text{MZI}}, \quad (3)$$

where  $f_{\text{north}}(\omega_{\text{SH}})$  is the field enhancement of the north resonator at the SH, while  $f_{\text{south}}(\omega_{\text{FH}})$  is the field enhancement of the south resonator at the FH,  $\sigma_{\text{SH(FH)}}$  and  $\kappa_{\text{SH(FH)}}$  are the coupling coefficients of the directional couplers at the SH (FH), linked by the relation  $\sigma_{\text{SH(FH)}}^2 + \kappa_{\text{SH(FH)}}^2 = 1$ , and  $\Delta k$  is the phase matching condition, which is:

$$\Delta k = k_{\text{SH}} - 2k_{\text{FH}} - \frac{2\pi}{\Lambda}, \quad (4)$$

where  $\Lambda$  is the poling period. The resonant field enhancement inside the  $i^{\text{th}}$  resonator can be expressed in term of quality factors as [30]:

$$|f_i(\omega_0)|^2 = \frac{4v_{\text{g},\omega_0} Q_{\text{L},\omega_0}^2}{\omega_0 L_i Q_{\text{C},\omega_0}}, \quad (5)$$

where  $i = \text{north, south}$ ,  $\omega_0 = \omega_{\text{SH}}, \omega_{\text{FH}}$  is the resonance frequency,  $L_i$  is the length of the  $i^{\text{th}}$  resonator,  $Q_{\text{L},\omega_0}$  and  $Q_{\text{C},\omega_0}$  are the loaded and coupling quality factors, respectively. In our structure, considered linearly uncoupled by setting  $\sigma_{\text{SH}} = \kappa_{\text{FH}} = 1$ , we have a nonlinear effective area  $A_{\text{eff}} = 1.34 \mu\text{m}^2$ , loaded quality factors  $Q_{\text{L,SH}} = 1.78 \times 10^6$  and  $Q_{\text{L,FH}} = 0.69 \times 10^6$ , coupling quality factors  $Q_{\text{C,SH}} = 9.69 \times 10^6$  and  $Q_{\text{C,FH}} = 3.05 \times 10^6$ , total length of the resonators  $L_{\text{SH}} = 1129 \mu\text{m}$  and  $L_{\text{FH}} = 1124 \mu\text{m}$ , and length of the Mach-Zehnder arm  $L_{\text{MZI}} = 361 \mu\text{m}$ . When the active AOP process sets the phase mismatch  $\Delta k = 0$ , inducing a  $\chi_{\text{eff}}^{(2)} = 0.1 \text{ pm/V}$ , we get for an injected power of  $P_{\text{FH}} = 300 \text{ mW}$  a generated power of  $P_{\text{SH}} \simeq 20 \text{ mW}$ , with a conversion efficiency  $\text{CE} \simeq 22\%/W$ .

**Experimental devices.** The devices used in this work were fabricated through a commercially available foundry service (Ligentec SA). The silicon nitride waveguides and resonators have a nominal cross-section of  $1 \times 0.8 \mu\text{m}^2$  and they are embedded in a silica cladding. Each fabricated photonic chip contains 69 devices (labeled “MZ1-MZ69”), all functional, designed to scan different values of north/south FSRs, to target different values of propagation loss in the two bands, and to compensate for fabrication imperfections.

After a first assessment of the linear properties of the devices fabricated, we focused our investigation on a single device (“MZ53”), which we used to obtain the results shown in this work. The selected device displays a total south (north) loop length of  $1123.83 \mu\text{m}$  ( $1129.186 \mu\text{m}$ ) for the FH (SH) optical path. The south resonator is coupled to the bus waveguide through a point coupler with  $0.67 \mu\text{m}$  gap, while the north resonator relies on a  $62.1 \mu\text{m}$  long directional coupler with  $0.3 \mu\text{m}$  gap to efficiently in- and out-couple light to the bus waveguide, tailored for a target propagation loss of  $0.2 \text{ dB/cm}$  and  $0.4 \text{ dB/cm}$  for the FH/SH bands respectively.

Both resonators use Euler bends to mitigate mode mixing, with an effective bend radius around  $30 \mu\text{m}$ .

The MZI section consists of two  $32 \mu\text{m}$  long directional couplers with a gap of  $0.3 \mu\text{m}$ . The upper arm of the MZI has a length of  $361.16 \mu\text{m}$  and the interferometer is unbalanced by  $2.197 \mu\text{m}$  to separately adjust the residual coupling of the FH and SH fields.

**Linear characterization.** To characterize the linear properties of the device(s), we coupled light from a tunable laser (Toptica CTL at FH, New Focus Velocity TLB at SH) to the chip using a lensed fiber. The sample contains inverse tapered waveguides, that provide an insertion loss between 2 and 3 dB per facet at the pump wavelength. Light is collected in free space using an aspheric lens and routed either to InGaAs/Si detectors or coupled to fiber and routed to an optical spectrum analyzer. Light at FH and SH is separated using a dichroic filter, while the input polarization is controlled to match the one of the fundamental TE mode. To perform linear scans, we sweep the laser wavelength and record the transmitted power using a fast photodiode. A fiber-based interferometer is used to calibrate the measurement to precisely assess the GVD. The transmission spectra are recorded for varying power of the south, north, and MZI heaters (Supplementary Note 1).

**SHG investigation and optimization of the generated power.** To investigate SHG, we proceed as follows. On a selected device, we first tune the MZI heater to maximize visibility and Q factor in the pump band: this is done to prevent the leakage of pump power towards the north resonator resonances, that are strongly overcoupled in the pump band and therefore act as a parasitic loss channel. We then amplify the pump using an erbium-doped fiber amplifier (EDFA) to obtain a typical power around  $320 \text{ mW}$  in the bus waveguide and tune it in resonance with the target south resonator mode. We then scan the north ring resonances from lower to higher frequencies by slowly ramping down the current driving the north heater. As soon as a nearly doubly resonant condition is matched, the onset for the AOP process occurs, highlighted by a sudden increase in the generated SH power, which settles to a stable value in a time ranging from few milliseconds to several seconds. Finally, we slightly optimize the three heaters’ currents to maximize the generated SH.

**TPM imaging.** For characterization of the inscribed  $\chi^{(2)}$  gratings, a high power femtosecond Ti:Sapphire laser is focused at the grating plane of the microresonator in an upright configuration. The focal spot is then raster-scanned across the plane while, in the meantime, its generated SH signal is monitored so that the (squared)  $\chi^{(2)}$  response is probed. From the periodicity retrieved, the original phase mismatch between the modes involved is inferred as:

$$\frac{2\pi}{\Lambda} = \frac{2\omega}{c} |n_{\text{eff}}^{\text{SH}} - n_{\text{eff}}^{\text{FH}}| \quad (6)$$

where  $\Lambda$  is the poling period,  $\omega$  is the pump angular frequency and  $n_{\text{eff}}^{\text{FH(SH)}}$  is the effective index of the FH (SH) mode. From simulations, we estimate  $\Lambda = 4.35 \mu\text{m}$ , in good agreement with the result shown in Fig. 2d.

## Acknowledgements

This work was funded by the European Research Council grant PISSARRO (ERC-2017-CoG 771647) and by the Swiss National Science Foundation (grant 214889). L.Z. and M.L. acknowledge support from PNRR MUR project PE0000023-NQSTI.

**Competing interests** The authors declare no competing interests.

## Data availability

The data and code that support the plots within this paper and other findings of this study are available from the corresponding authors upon reasonable request.

- \* Now at: Dipartimento di Fisica, Università di Pavia, Via A. Bassi 6, 27100 Pavia, Italy; [marco.clementi01@unipv.it](mailto:marco.clementi01@unipv.it)
- [1] R. W. Boyd, *Nonlinear Optics*, 4th ed. (Academic Press, 2020).
  - [2] O. Svelto, *Principles of Lasers* (Springer US, 2010).
  - [3] P. Campagnola, Second harmonic generation imaging microscopy: Applications to diseases diagnostics, *Analytical Chemistry* **83**, 3224 (2011).
  - [4] R. Trebino, *Frequency-Resolved Optical Gating: The Measurement of Ultrashort Laser Pulses* (Springer US, Boston, MA, 2000).
  - [5] Y. R. Shen, Optical second harmonic generation at interfaces, *Annual Review of Physical Chemistry* **40**, 327 (1989).
  - [6] P. G. Kwiat, K. Mattle, H. Weinfurter, A. Zeilinger, A. V. Sergienko, and Y. Shih, New high-intensity source of polarization-entangled photon pairs, *Physical Review Letters* **75**, 4337 (1995).
  - [7] J. U. Fürst, D. V. Strekalov, D. Elser, M. Lassen, U. L. Andersen, C. Marquardt, and G. Leuchs, Naturally phase-matched second-harmonic generation in a whispering-gallery-mode resonator, *Physical Review Letters* **104**, 153901 (2010).
  - [8] J. Wang, M. Clementi, M. Minkov, A. Barone, J.-F. Carlin, *et al.*, Doubly resonant second-harmonic generation of a vortex beam from a bound state in the continuum, *Optica* **7**, 1126 (2020).
  - [9] J. Lu, M. Li, C.-L. Zou, A. Al Sayem, and H. X. Tang, Toward 1% single-photon anharmonicity with periodically poled lithium niobate microring resonators, *Optica* **7**, 1654 (2020).
  - [10] A. W. Bruch, X. Liu, X. Guo, J. B. Surya, Z. Gong, *et al.*, 17 000%/W second-harmonic conversion efficiency in single-crystalline aluminum nitride microresonators, *Applied Physics Letters* **113**, 131102 (2018).
  - [11] P. S. Kuo, J. Bravo-Abad, and G. S. Solomon, Second-harmonic generation using  $\bar{4}$ -quasi-phasing in a GaAs whispering-gallery-mode microcavity, *Nature Communications* **5**, 1 (2014).
  - [12] D. P. Lake, M. Mitchell, H. Jayakumar, L. F. dos Santos, D. Curic, and P. E. Barclay, Efficient telecom to visible wavelength conversion in doubly resonant gallium phosphide microdisks, *Applied Physics Letters* **108**, 031109 (2016).
  - [13] D. M. Lukin, C. Dory, M. A. Guidry, K. Y. Yang, S. D. Mishra, R. Trivedi, M. Radulaski, S. Sun, D. Ver-cruysse, G. H. Ahn, and J. Vučković, 4H-silicon-carbide-on-insulator for integrated quantum and nonlinear photonics, *Nature Photonics* **14**, 330 (2020).
  - [14] J. Liu, G. Huang, R. N. Wang, J. He, A. S. Raja, *et al.*, High-yield, wafer-scale fabrication of ultralow-loss, dispersion-engineered silicon nitride photonic circuits, *Nature Communications* **12**, 2236 (2021).
  - [15] A. Billat, D. Grassani, M. H. P. Pfeiffer, S. Kharitonov, T. J. Kippenberg, *et al.*, Large second harmonic generation enhancement in  $\text{Si}_3\text{N}_4$  waveguides by all-optically induced quasi-phase-matching, *Nature Communications* **8**, 1016 (2017).
  - [16] M. A. Porcel, J. Mak, C. Taballione, V. K. Schermerhorn, J. P. Epping, *et al.*, Photo-induced second-order nonlinearity in stoichiometric silicon nitride waveguides, *Optics Express* **25**, 33143 (2017).
  - [17] D. D. Hickstein, D. R. Carlson, H. Mundoor, J. B. Khurgin, K. Srinivasan, D. Westly, A. Kowligy, I. I. Smalyukh, S. A. Diddams, and S. B. Papp, Self-organized nonlinear gratings for ultrafast nanophotonics, *Nature Photonics* **13**, 494 (2019).
  - [18] O. Yakar, E. Nitiss, J. Hu, and C.-S. Brès, Generalized coherent photogalvanic effect in coherently seeded waveguides, *Laser and Photonics Reviews*, 2200294 (2022).
  - [19] X. Lu, G. Moille, A. Rao, D. A. Westly, and K. Srinivasan, Efficient photoinduced second-harmonic generation in silicon nitride photonics, *Nature Photonics* **15**, 131 (2021).
  - [20] E. Nitiss, J. Hu, A. Stroganov, and C.-S. Brès, Optically reconfigurable quasi-phase-matching in silicon nitride microresonators, *Nature Photonics* **16**, 134 (2022).
  - [21] E. Nitiss, B. Zabelich, O. Yakar, J. Liu, R. N. Wang, T. J. Kippenberg, and C.-S. Brès, Broadband quasi-phase-matching in dispersion-engineered all-optically poled silicon nitride waveguides, *Photonics Research* **8**, 1475 (2020).
  - [22] M. Clementi, E. Nitiss, J. Liu, E. Durán-Valdeiglesias, S. Belahsene, H. Debrégeas, T. J. Kippenberg, and C.-S. Brès, A chip-scale second-harmonic source via self-injection-locked all-optical poling, *Light: Science & Applications* **12**, 296 (2023).
  - [23] B. Li, Z. Yuan, W. Jin, L. Wu, J. Guo, Q.-X. Ji, A. Feshali, M. Paniccia, J. E. Bowers, and K. J. Vahala, High-coherence hybrid-integrated 780 nm source by self-injection-locked second-harmonic generation in a high-q silicon-nitride resonator, *Optica* **10**, 1241 (2023).
  - [24] E. Nitiss, B. Zabelich, J. Hu, A. Stroganov, and C.-S. Brès, Tunable photo-induced second-harmonic generation in a mode-engineered silicon nitride microresonator, *Optics Express* **31**, 14442 (2023).
  - [25] S. Miller, K. Luke, Y. Okawachi, J. Cardenas, A. L. Gaeta, and M. Lipson, On-chip frequency comb generation at visible wavelengths via simultaneous second- and third-order optical nonlinearities, *Optics Express* **22**, 26517 (2014).
  - [26] J. Hu, E. Nitiss, J. He, J. Liu, O. Yakar, W. Weng, T. J. Kippenberg, and C.-S. Brès, Photo-induced cascaded harmonic and comb generation in silicon nitride microresonators, *Science Advances* **8**, 2203.15889 (2022).
  - [27] X. Guo, C.-L. Zou, H. Jung, Z. Gong, A. Bruch, L. Jiang, and H. X. Tang, Efficient generation of a near-visible frequency comb via cherenkov-like radiation from a kerr microcomb, *Physical Review Applied* **10**, 014012 (2018).
  - [28] Y. He, Q.-F. Yang, J. Ling, R. Luo, H. Liang, M. Li, B. Shen, H. Wang, K. Vahala, and Q. Lin, Self-starting bi-chromatic  $\text{LiNbO}_3$  soliton microcomb, *Optica* **6**, 1138 (2019).
  - [29] D. J. Wilson, K. Schneider, S. Hönl, M. Anderson, Y. Baumgartner, L. Czornomaz, T. J. Kippenberg, and P. Seidler, Integrated gallium phosphide nonlinear photonics, *Nature Photonics* **14**, 57 (2020).
  - [30] M. Menotti, B. Morrison, K. Tan, Z. Vernon, J. E. Sipe, and M. Liscidini, Nonlinear coupling of linearly uncoupled resonators, *Physical Review Letters* **122**, 013904 (2019).

- [31] K. Tan, M. Menotti, Z. Vernon, J. E. Sipe, M. Liscidini, and B. Morrison, Stimulated four-wave mixing in linearly uncoupled resonators, *Optics Letters* **45**, 873 (2020).
- [32] F. A. Sabattoli, H. El Dirani, L. Youssef, F. Garrisi, D. Grassani, L. Zatti, C. Petit-Etienne, E. Pargon, J. E. Sipe, M. Liscidini, C. Sciancalepore, D. Bajoni, and M. Galli, Suppression of parasitic nonlinear processes in spontaneous four-wave mixing with linearly uncoupled resonators, *Physical Review Letters* **127**, 033901 (2021).
- [33] F. A. Sabattoli, H. El Dirani, L. Youssef, L. Gianini, L. Zatti, F. Garrisi, D. Grassani, C. Petit-Etienne, E. Pargon, J. E. Sipe, M. Liscidini, C. Sciancalepore, D. Bajoni, and M. Galli, Nonlinear coupling of linearly uncoupled resonators through a mach–zehnder interferometer, *Applied Physics Letters* **121**, 201101 (2022).
- [34] L. Zatti, N. Bergamasco, E. Lomonte, F. Lenzini, W. Pernice, and M. Liscidini, Spontaneous parametric downconversion in linearly uncoupled resonators, *Optics Letters* **47**, 1766 (2022).
- [35] L. Zatti, J. E. Sipe, and M. Liscidini, Generation of photon pairs by spontaneous four-wave mixing in linearly uncoupled resonators, *Phys. Rev. A* **107**, 013514 (2023).
- [36] E. Nitiss, T. Liu, D. Grassani, M. Pfeiffer, T. J. Kippenberg, *et al.*, Formation rules and dynamics of photoinduced  $\chi(2)$  gratings in silicon nitride waveguides, *ACS Photonics* **7**, 147 (2020).
- [37] J. Zhou, J. Hu, M. Clementi, O. Yakar, E. Nitiss, A. Stroganov, and C.-S. Brès, *Self-organized spatiotemporal quasi-phase-matching in microresonators* (2024), [arXiv:2407.15587](https://arxiv.org/abs/2407.15587).
- [38] X. Xue, M. Qi, and A. M. Weiner, Normal-dispersion microresonator kerr frequency combs, *Nanophotonics* **5**, 244 (2016).
- [39] P.-K. Chen, I. Briggs, C. Cui, L. Zhang, M. Shah, and L. Fan, Adapted poling to break the nonlinear efficiency limit in nanophotonic lithium niobate waveguides, *Nature Nanotechnology* **19**, 44 (2024).
- [40] J. Lu, J. B. Surya, X. Liu, A. W. Bruch, Z. Gong, Y. Xu, and H. X. Tang, Periodically poled thin-film lithium niobate microring resonators with a second-harmonic generation efficiency of 250,000%/W, *Optica* **6**, 1455 (2019).
- [41] X. Guo, C.-L. Zou, and H. X. Tang, Second-harmonic generation in aluminum nitride microrings with 2500%/W conversion efficiency, *Optica* **3**, 1126 (2016).
- [42] Ó. B. Helgason, M. Girardi, Z. Ye, F. Lei, J. Schröder, and V. Torres-Company, Surpassing the nonlinear conversion efficiency of soliton microcombs, *Nature Photonics* **17**, 992 (2023).
- [43] Q. X. Ji, P. Liu, W. Jin, J. Guo, L. Wu, Z. Yuan, J. Peters, A. Feshali, M. Paniccia, J. E. Bowers, and K. J. Vahala, Multimodality integrated microresonators using the Moiré speedup effect, *Science (New York, N.Y.)* **383**, 1080 (2024).
- [44] Y. Zhang, M. Menotti, K. Tan, V. D. Vaidya, D. H. Mahler, L. G. Helt, L. Zatti, M. Liscidini, B. Morrison, and Z. Vernon, Squeezed light from a nanophotonic molecule, *Nature Communications* **12**, 2233 (2021).
- [45] D. Nigro, M. Clementi, C.-S. Brès, M. Liscidini, and D. Gerace, Single-photon nonlinearities and blockade from a strongly driven photonic molecule, *Optics Letters* **47**, 5348 (2022).
- [46] E. Sahin, B. Zabelich, O. Yakar, E. Nitiss, J. Liu, R. N. Wang, T. J. Kippenberg, and C.-S. Brès, Difference-frequency generation in optically poled silicon nitride waveguides, *Nanophotonics* **10**, 1923 (2021).
- [47] R. Dalidet, F. Mazeas, E. Nitiss, O. Yakar, A. Stroganov, S. Tanzilli, L. Labonté, and C.-S. Brès, Near perfect two-photon interference out of a down-converter on a silicon photonic chip, *Optics Express* **30**, 11298 (2022).
- [48] M. Liscidini, L. G. Helt, and J. E. Sipe, Asymptotic fields for a hamiltonian treatment of nonlinear electromagnetic phenomena, *Physical Review A* **85**, 013833 (2012).
- [49] Z. Yang, M. Liscidini, and J. E. Sipe, Spontaneous parametric down-conversion in waveguides: A backward heisenberg picture approach, *Physical Review A* **77**, 033808 (2008).



# Supplementary Information for: Ultrabroadband Resonant Frequency Doubling on a Photonic Chip

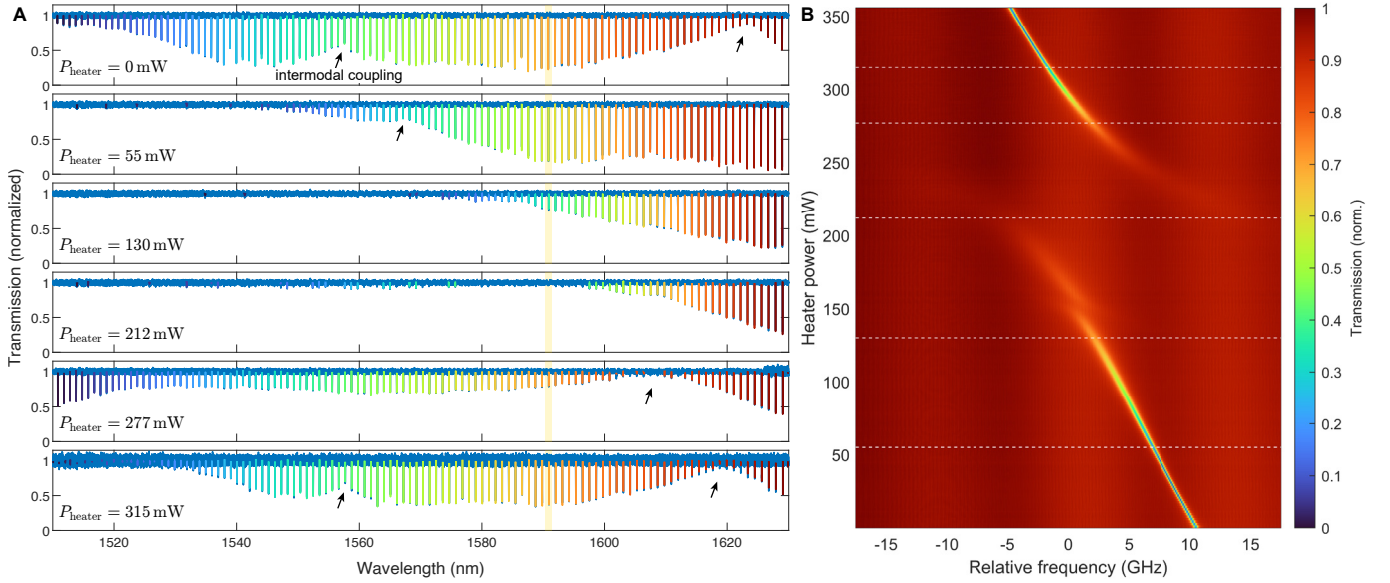
Marco Clementi,<sup>1,\*</sup> Luca Zatti,<sup>2</sup> Ji Zhou,<sup>1</sup> Marco Liscidini,<sup>2</sup> and Camille-Sophie Brès<sup>1</sup>

<sup>1</sup>Photonic Systems Laboratory, École Polytechnique Fédérale de Lausanne, 1015 Lausanne, Switzerland

<sup>2</sup>Dipartimento di Fisica, Università di Pavia, Via A. Bassi 6, 27100 Pavia, Italy

(Dated: December 5, 2024)

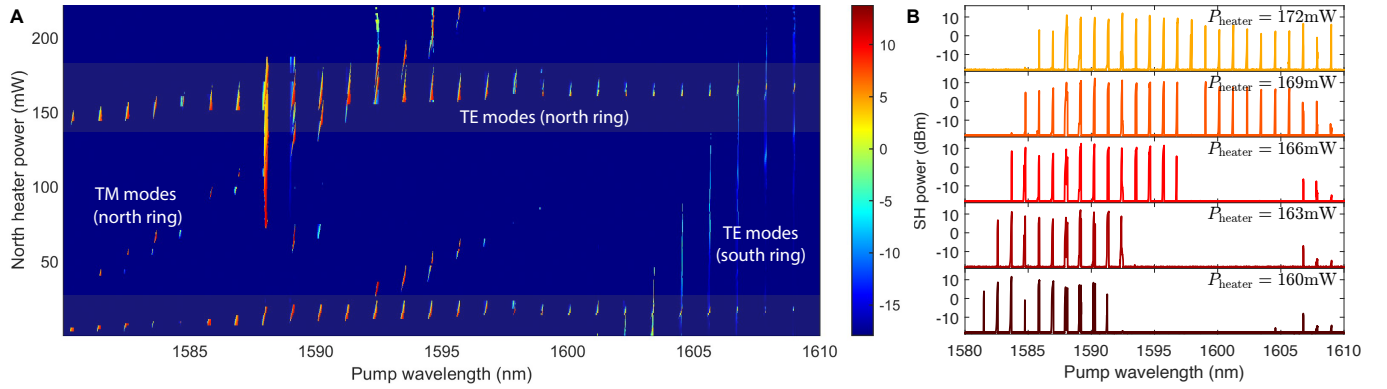
## Supplementary Note 1: Effect of the MZI tuning



Supplementary Figure 1. **Optimization of the linear uncoupling through MZI tuning.** **a.** Linear transmission spectra for increasing values of the MZI heater power. The maximum resonance visibility is obtained when the linear coupling is minimized. The features highlighted by black arrows are attributed to intermodal coupling. **b.** High resolution transmission spectra for a resonance around 1590.9 nm (shaded area in panel **a**). The highest Q and visibility are obtained for a heater power of either 35 mW or 340 mW. Horizontal dashed lines mark the heater powers shown in panel **a**.

Here we discuss the effect of residual linear coupling between the north and south resonators and the role of the MZI heater. Supplementary Figure 1a shows the linear transmission spectra from the bus waveguide of the south resonator in the pump band for varying values of the MZI heater power. Ideally, in the complete absence of linear coupling the spectrum should display a set of nearly critically coupled resonances. Fabrication imperfections and the wavelength dependence of the directional couplers composing the MZI structure make it deviate from the ideal 100:0 splitting ratio, introducing a small residual linear coupling in the pump band. This manifests as a lower resonance visibility and broader linewidth in some regions of the transmission spectrum: the north resonator is indeed strongly overcoupled in the pump band, and therefore acts as a loss channel whenever some residual linear coupling exists. Such leak of power towards the north resonator can also be observed through collection from the corresponding (north) bus waveguide. We mitigate this issue by acting on the MZI heater, which can be tuned to reach nearly ideal linear uncoupling in the desired spectral region, as shown in Supplementary Figure 1a. In Supplementary Figure 1b, a high resolution scan focusing on a single resonance around 1591 nm reveals, as an example, optimal visibility and narrowest linewidth for a heater power around 35 mW. For higher powers, the resonance undergoes a linewidth broadening, while the narrow linewidth is recovered for a heater power around 340 mW. The resonance also displays an anticrossing-type behavior, which we attribute to the hybridization with the north resonator low-Q  $TE_{00}$  resonance. Finally, we note that the transmission spectra also display local features associated with lower visibility and broader linewidth (black arrows). We attribute these to weak intermodal coupling between the south resonator  $TE_{00}$  mode and other mode families in the north resonator.

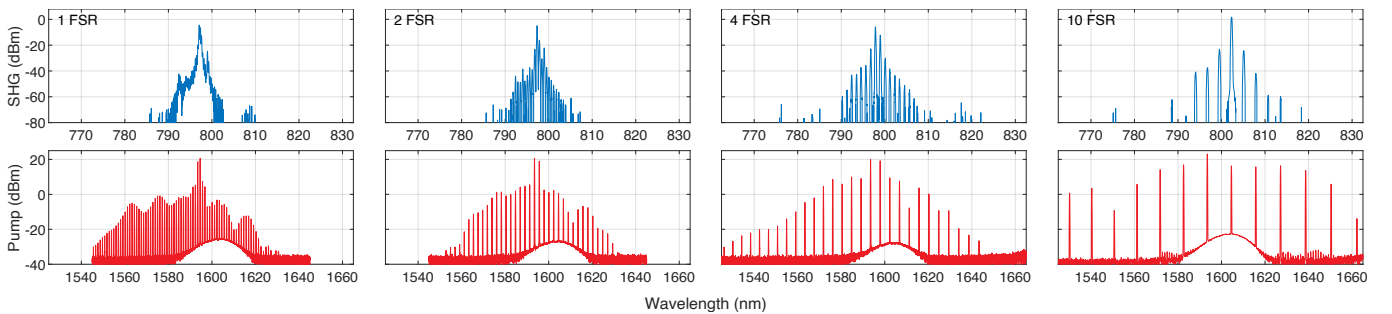
## Supplementary Note 2: Mapping of the AOP process



Supplementary Figure 2. **Reconfiguration of the nonlinear interaction.** **a.** SHG map as a function of pump wavelength and north heater power. The trends highlighted correspond to doubly resonant SHG involving the  $TE_{00}$ - $TE_{00}$  mode pair. **b.** Detail from panel **a** showing typical SHG spectra for various values of the pump north heater power.

To gather insight on the properties of the developed device, we carry out an extensive mapping of the AOP process across the L band [? ?]. By slowly ( $100 \text{ pm s}^{-1}$ ) scanning the pump wavelength while keeping constant its power, we record the generated SH power for different driving conditions of the north heater. The results, shown in Supplementary Figure 2a, highlight the presence of several mode families at the SH, that can be visually identified as linear trends in the two-dimensional map. In particular, the target mode family (i.e. the SH  $TE_{00}$  modes of the north resonator) are represented by horizontal trends (shaded regions). This is expected since the FSR of this mode family at the pump is matched with the one of the north ring at the SH: the result is that, for the correct value of north heater power, efficient SHG can occur across multiple resonances at the time. Examples of SHG spectra for this mode family are shown in Supplementary Figure 2b. Other linear trends are visible on the AOP map: we identify a first one associated with the AOP of  $TM_{00}$  modes in the north resonator, and a second one with AOP of the  $TE_{00}$  modes of the south ring, as revealed by polarization analysis of the generated SH in combination with imaging of the device during the AOP process.

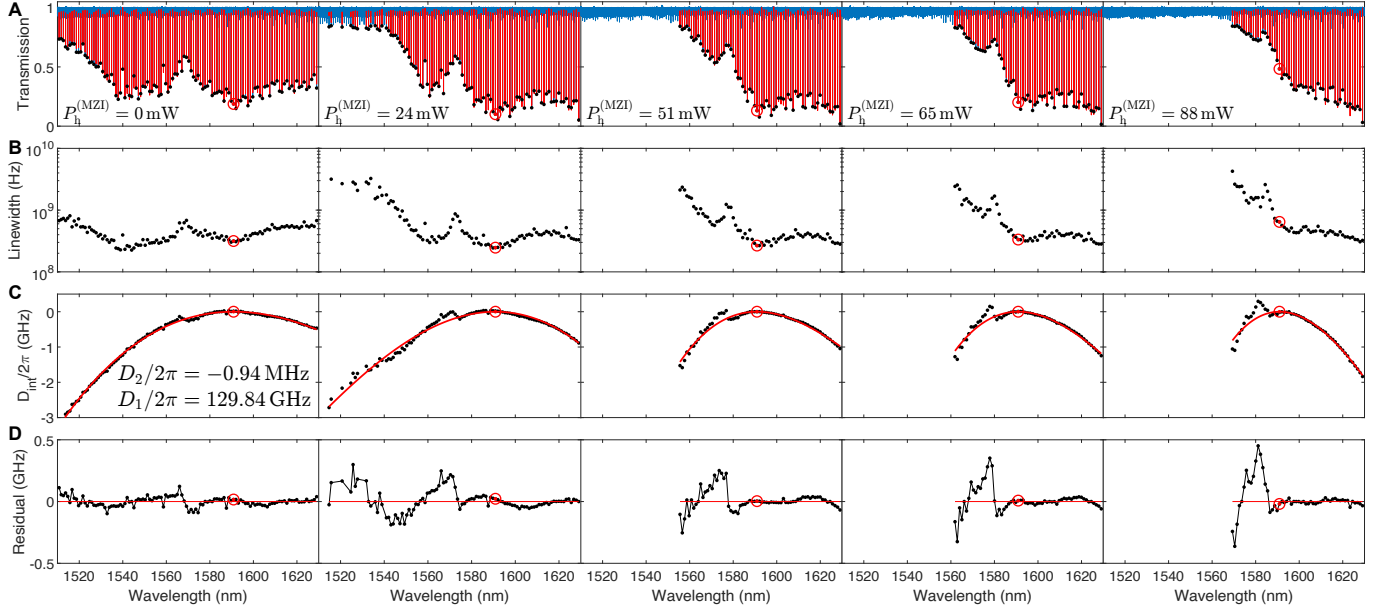
## Supplementary Note 3: Higher order stimulated FWM comb



Supplementary Figure 3. **Multi-FSR comb.** Dependence of the stimulated FWM comb on the pump lines spacing, as a multiple of the south resonator FSR.

Supplementary Figure 3 shows the evolution of the stimulated FWM comb and its upconverted spectrum for varying values of the FSR. Here, a dual-tone pump is used as shown in Fig. 4 of the main text, while the pump lines spacing is tuned to an integer multiple of the south resonator's FSR. It can be noted that, while the pump comb extent and pump-to-line CE increases for increasing values of the spacing, the extend of the upconverted spectrum barely changes. We attribute this phenomenological observation to the residual mismatch between the south and north resonators FSR in the respective bands.

## Supplementary Note 4: Resonator dispersion



Supplementary Figure 4. **Evolution of the resonator dispersion and linewidth for varying MZI heater power.** **a.** Low power, normalized transmission spectra. Red curves are Lorentzian fits of the recorded resonances and black dots indicate the minimum transmission. The red dot marks the pump resonance used for Kerr comb generation, around 1591 nm. **b.** Linewidth (full-width at half-maximum) values retrieved from best fit. **c.** Integrated dispersion profile. The red curve is a fit of the recorded data up to third order according with Eq. (1). **d.** Residual from best fit of data in panel **c**. Note the intensification and contextual redshift of the perturbation (associated with broader linewidth and shifted GVD profile) for increasing heater power.

Here we investigate the formation mechanism for the comb states shown in Fig. 5 of the main text. Supplementary Figure 4 shows transmission spectra for varying values of the MZI heater power. The laser wavelength was calibrated using a SMF28 fiber loop of known length and GVD. First, we note that the resonances visibility and linewidth are strongly affected by the tuning of the MZI heater (Supplementary Figure 4a-b). For a heater power comparable with that used to generate the MI comb (around 65 mW, fourth column), a high visibility is achieved for the pump resonance, while resonances at lower wavelength display broader linewidth. This narrow wavelength dependence of the visibility relaxes the conditions required for the pump comb generation, while not significantly affecting the threshold. A second factor affecting the comb formation can be deduced from the measurements of integrated dispersion relative to the pump resonance frequency (Supplementary Figure 4c), defined as:

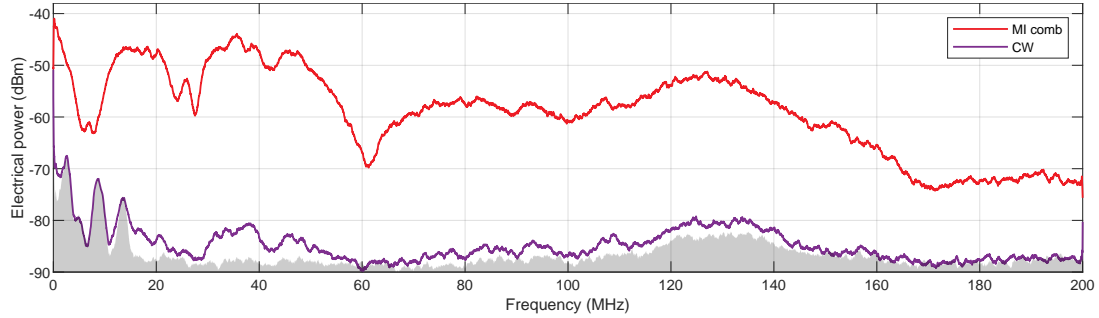
$$D_{\text{int}}(\mu) = \omega_{\mu} - \omega_0 - D_1\mu = \sum_{k \geq 2} \frac{D_k}{k!} \mu^k \quad (1)$$

where  $\omega_{\mu}/2\pi$  is the frequency of the  $\mu$ -th order resonance with respect to the pump,  $D_1/2\pi = 129.84$  GHz is the microresonator's FSR, and  $D_2/2\pi = -0.94$  MHz is the group-velocity dispersion parameter, as determined from best fit of data at low heater power. This indicates that the resonator is in normal GVD regime. On the other hand, the presence of an anti-crossing type perturbation, also marked by a local increase of the resonances linewidth, alters the otherwise quadratic trend, facilitating the formation of MI combs [? ?]. We note that the entity of this perturbation increases for increasing values of heater power, which we attribute to the increased linear coupling between the mode families of the resonators involved, while its spectral position gradually redshifts, increasing its effect on the pump resonance. The optimal condition experimentally found for MI comb generation is a compromise between the resonance shift imparted by such resonance coupling and its detrimental effect on the pump threshold associated with linewidth broadening.



## Supplementary Note 5: Noise of the modulation instability comb

Supplementary Figure 5 shows an electrical noise spectrum associated with the generated modulation instability comb shown in Fig. 5a of the main text. Here, light in the FH band at the output of the south resonator is sent to a fast photodiode and the photodetected current is routed to an electrical spectrum analyser (ESA), where the electrical noise spectrum is recorded. Compared with the noise spectrum of the continuous wave (CW) comb pump alone, which is close to the detector's noise floor, the generated comb yields highly noisy spectrum, which is typical of MI states. This observation confirms the incoherent nature of the generated comb.



Supplementary Figure 5. **Modulation instability comb noise spectrum.** Electrical spectrum analyzer spectra of a generated comb spectrum at FH (red) and of the pump out of resonance (purple) for the generated MI comb state shown in Fig. 5a of the main text. The gray shaded area represents the detector noise floor.